Available online at www.sciencedirect.com
ScienceDirect
Engineering Fracture Mechanics 75 (2008) 1666–1683
Engineering Fracture Mechanics
www.elsevier.com/locate/engfracmech

Analysis of FRP–concrete debonding via boundary integral equations

F. Freddi [a,*], M. Savoia [b]

[a] Department of Civil-Environmental Engineering and Architecture, University of Parma, Italy
[b] DISTART-Structural Engineering, University of Bologna, Italy

Received 22 May 2006; received in revised form 14 May 2007; accepted 24 May 2007
Available online 27 June 2007

Abstract

The problem of debonding of FRP plates glued over a concrete element is studied making use of boundary integral equations. Mode II cohesive crack model is adopted for the interface, whereas linear elasticity is used for the two materials outside the process zone. Symmetric Galerkin boundary element method is used, adopting the arc-length technique to follow the equilibrium path beyond its critical point. It is shown that, due to the presence of a softening branch in shear stress-slip law, the behavior of a specimen undergoing debonding may be strongly non-linear, and is associated with a very brittle failure mechanism. For bond lengths longer than minimum anchorage length, a snap-back branch typically occurs after the attainment of the maximum force. Two different test setups have been numerically simulated and results in good agreement with experimental tests are found.

Keywords: SG-BEM; Cohesive interface; FRP–concrete delamination; Arc-length method

1. Introduction

Debonding is the most important failure mode in reinforced concrete structures strengthened by external bonding of fiber reinforced polymer (FRP) plates or sheets, and received great attention in recent years. Debonding may arise from extremities of reinforcement or from intermediate cracks in the concrete due to flexure [62]. In both cases, axial force must be transmitted from FRP external reinforcement to concrete, and debonding occurs prevailingly in mode II condition, due to very high shear stresses at the interface level and relatively small shear strength of the concrete cover. In other cases, debonding may start from diagonal shear cracks in concrete, with displacement discontinuity over concrete support causing very high normal (peeling) stresses associated with shear stresses (see [23,68,69,24]), and mixed mode fracture occurs.

As far as the problem of modelling of FRP–concrete debonding is concerned, most common procedures can be divided into three main groups, those based on stress analysis, on linear elastic fracture mechanics

* Corresponding author. Tel.: +39 0521905917.
E-mail address: francesco.freddi@unipr.it (F. Freddi).

0013-7944/$ - see front matter © 2007 Elsevier Ltd. All rights reserved.
doi:10.1016/j.engfracmech.2007.05.016

(LEFM) or on cohesive crack models. In the first case, FRP–concrete interface is modelled as a linear elastic layer, and debonding occurs if interfacial stress reaches shear strength of the interface [52,37], for a review see [60]. The method is very simple, and can be used for both bond–slip models and 2D FEM domain discretizations. Nevertheless, experimental results showed that most of load is transmitted in mode II condition in non-linear range for the interface (see Sections 2 and 4). Then, in order to predict at least the order of magnitude of debonding load, unreasonably high values of interface strength must be assumed adopting a stress-based criterion for debonding. LEFM has been widely adopted to model delamination problems. It relies on the assumption of the existence of initial defects or cracks and cannot be applied directly without initial delamination. Techniques such as virtual crack closure [32,53,72], *J*-integral [50] and virtual crack extension [29] are some of the most used procedures. Applications of methods based on LEFM to FRP–concrete delamination can be found in [61,12,49]. More recently, models based on a cohesive or damage zone for the simulation of fracture process are becoming more and more popular [13,4,46,2,71,18,26]. The basic idea for such models can be traced back to [19,6,7,30]. In the *cohesive crack model*, the fracture process zone is modelled as a fictitious crack; strain localization is idealized as a crack opening and sliding, related to cohesive tractions by means of constitutive relations. Advantages of such models are their simplicity and unification of crack initiation and growth within one model.

Cohesive crack models are widely used to study FRP–concrete debonding. When mode II fracture is dominant (such as in the case of end debonding), numerical models are typically based on shear stress–tangential slip interface laws (see [35] for a review of existing bond–slip models). In this cases, relative displacement between FRP reinforcement and concrete is lumped within the interface layer, whose constitutive law collects all compliance contributions of adhesive and external concrete layer. Experimental studies clearly suggest that debonding typically occurs a few millimetres inside the concrete specimen, but with this definition of FRP–concrete interface, debonding is treated as occurring along the interface, and linear elastic laws can be adopted for concrete (see Section 2). Mode II interface laws are usually obtained from post-processing of experimental results [57,43,66,22]. In [36] it is shown that mode II bond–slip interface laws can be derived by a meso-scale FE model by adopting mode I tension-softening law for damaged concrete during debonding.

Some analytical and numerical solutions have been derived by adopting mode II interface laws and simple shear-lag models (as initially proposed by [65]), where axial deformation only is considered and bending of concrete element and FRP–concrete reinforcement are neglected. Bilinear local mode II bond–slip interface law has been used in [68,70] to study shear stress transfer and fracture propagation from FRP–concrete reinforcement extremities, and in [42,63] to study intermediate debonding. Power fractional interface law and finite-difference solution technique have been used in [56,21]. In this case, mode II bond–slip interface law has been calibrated starting from experimental data on delamination tests. This law includes non-linear behavior of adhesive layer and external cover of concrete subjected to very high shear stress (see Section 2).

More complete analyses require concrete and external reinforcement be considered as two-dimensional (or three-dimensional) bodies. In this framework, finite element method is the most widely used (see for instance [33,16,36]). Boundary element methods [10] are also very attractive for FRP–concrete debonding problems, because non-linear behavior can be localized in a non-linear interface law, whereas concrete element and reinforcement can be considered as linear elastic bodies.

In case displacement discontinuity locus is not established a priori and fracture propagation occurs inside the concrete specimen, with unknown directions, other numerical techniques can be adopted such as the dual boundary element method, as detailed in [3].

In the present paper, a fully symmetric Galerkin boundary element method is used to study the problem of mode II debonding of a FRP–concrete plate bonded on a concrete support. The incremental boundary integral equations (BIEs) for the problem of several elastic domains connected by cohesive non-linear interfaces adopted in the present study have been originally proposed in [54], and are shortly summarized in Section 3. Stemming from displacement and traction BIEs for a single domain [31,27], the problem is formulated in terms of displacement fields **u**, **v**, traction field **p** and displacement discontinuity field **w** along the interfaces. Displacement discontinuities are related to cohesive tractions by means of a holonomic non-linear interface law. In the case of a symmetric cohesive law, the integral operator governing the problem is proved to be linear with respect to the unknown rate fields and symmetric with respect to a suitable bilinear form. Therefore, the boundary integral problem admits a variational formulation and its solution is a critical point of a quadratic

functional. As a main consequence of this variational framework, Galerkin approximation scheme [41] can be adopted. Differently from [15], where the partial symmetric formulation proposed for multi-zone problems implies an ad-hoc treatment of the non-symmetric part of the discrete matrix, the fully symmetric technique adopted leads to clear advantage from theoretical and computational points of view.

Main guidelines of the proposed incremental algorithm, detailed in [25,1], are given in Section 3. Due to softening nature of the interface law, debonding phenomenon is characterized by a highly non-linear behavior. Hence, in the proposed numerical scheme, Riks arc-length technique with local control has been used as solution algorithm.

Several numerical simulations have been performed, concerning two different setups of mode II debonding tests of FRP plates bonded on concrete substrate. Due to the presence of a sharp softening branch in shear stress-slip law, debonding phenomenon may be strongly non-linear, and snap-back equilibrium branch may be present after the attainment of maximum load. This circumstance confirms the very brittle failure mechanism associated with FRP debonding. Nevertheless, with the proposed algorithm crack nucleation and growth can be numerically followed, up to complete debonding. Numerical results are found in good agreement with experimental results reported in the literature.

It is shown that the proposed symmetric Galerkin boundary element technique provides for a powerful tool for solving cohesive interface problems, giving correct values of debonding forces for different anchorage lengths and distributions of FRP strains along the bond length.

2. Mode II non-linear interface law

2.1. Mode II shear fracture for FRP–concrete debonding

In the so-called cohesive crack model, see [6,7,30], the fracture process zone is modelled as a fictitious crack, constituting a transition zone between the un-cracked zone and the traction-free crack. Strain localization is idealized as a crack opening and sliding, and cohesive forces (normal and shear) are related to displacement discontinuities by softening laws. The area under stress–displacement relation represents the fracture energy required to create a fully developed crack of unit length.

According to theoretical fracture mechanics, fracture propagation direction is governed by the criterion of the maximum energy release rate, see for instance [9], as a consequence of basic laws of thermodynamics. Then, cracks in concrete specimens are usually related to tensile failure (mode I fracture energy being the minimum), and crack propagation direction from the notch tip is taken as normal to the maximum principal tensile stress according to [20]. Also in shear-loaded beams with a start notch in the mode II direction [5], if a wide zone of beam is subject to shear, crack typically deviates from mode II fracture direction to that orthogonal to maximum principal stress. Nevertheless, mode II (or shear) fracture failures may occur when a narrow region is subject to high shear stresses. For instance, in [8], shear fracture has been observed in shear-loaded beams with starting notches similar to those tested by [5], but with much smaller distance between applied shear forces: in this case, according to the criterion of the maximum energy release rate, cracks cannot deviate into a low stress zone of the material, because they would release little energy.

As clearly described in [8], shear fracture initially forms as a zone of inclined tensile microcracks. Full shearing failure then requires inclined struts between microcracks be finally crushed in compression. The completely different failure mechanism at the meso-level explains why mode II fracture energy G_f^{II} is far larger than mode I (G_f^{I}), even 25 times larger according to [8]. For concrete specimens, G_f^{I} can be considered as a basic material constant whereas G_f^{II} is not, since it can be calculated on the basis of G_f^{I}, tensile concrete strength and crack band width.

When a plate is bonded to a concrete specimen and is subject to axial load up to failure, mode II shear failure occurs. In fact, only a small layer of concrete close to interface is subject to very high shear stresses, and criterion of the maximum release rate requires fracture propagates along it. Failure mechanism is similar as described before: inclined microcracks forms in the small external layer of concrete because tensile strength is much lower than adhesive, and final shear crack typically occurs few millimetres below adhesive-concrete interphase. Correspondingly, fracture energy is much higher than mode I fracture energy of concrete, as confirmed by several experimental studies. Failure phenomenon at the meso-scale level has been studied in [36],

where a mode II shear stress-slip law has been derived starting from tension-softening constitutive law for concrete. Similar results were also obtained by [16] by adopting a plastic damage model for concrete epoxy interface.

Moreover, mode II fracture energy is usually higher than for plain concrete, due to penetration of adhesive in the concrete external layer, so depending also on adopted adhesive characteristics and concrete surface preparation before adhesive application [64,44,58]. For this reason, direct shear tests are recommended to calibrate mode II non-linear interface laws.

2.2. Mode II interface laws from shear tests

Mode II interface laws can be obtained from experimental strain gauge measures along FRP reinforcement in a shear test performed up to complete debonding (see [35] for a review of existing models). These laws then include overall compliance of the support, i.e. of both adhesive and concrete cover subject to high shearing deformation: for low slip values, linear compliances of both adhesive and concrete cover are included; for high slips, failure and subsequent post-failure softening behaviors, occurring in concrete cover, are also modelled at the interface level. Hence, these laws are appropriate for models based on assumption of plane profile of deformation over concrete height (called bond–slip models in the following), i.e., not including localized shear strains close to the interface, because this deformation mode is already modelled at the interface level.

A mode II power fractional interface law has been recently proposed in [22]. It has been obtained by post-processing experimental data of delamination tests, and gives the local bond stress τ as a function of slip s (see Fig. 1):

$$\frac{\tau}{\bar{\tau}} = \frac{s}{\bar{s}} \frac{n}{(n-1) + (|s|/\bar{s})^n} \tag{1}$$

where $(\bar{\tau}, \bar{s})$ denote peak shear stress and corresponding slip and $n > 2$ is a free parameter mainly governing the softening branch, where shear stress transmission is due to aggregate interlock.

In [40,58] it has been shown that, if boundary effects are avoided in tests, parameters of interface law are independent of geometry of the specimens and test setup, but they are a function of concrete strength, surface preparation and reinforcement type (FRP plates or sheets).

2.3. Mode II interface laws for 2D numerical simulations

Interface laws (1) cannot be used directly for problems where concrete specimen domain is discretized as a 2D elastic body (such as FEM of BEM), since elastic concrete deformation close to the interface would be

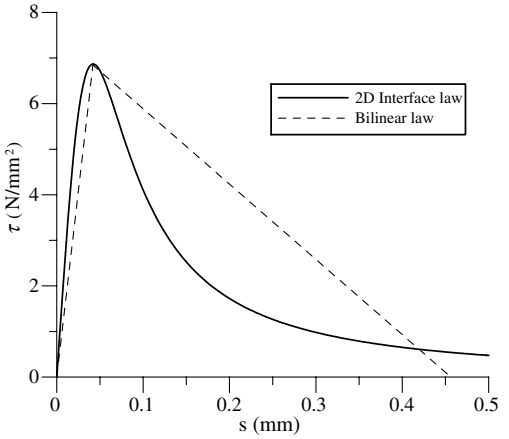

Fig. 1. Mode II non-linear FRP–concrete interface laws: the power fractional law and a bilinear law. The parameters adopted for power fractional law are: $\bar{\tau} = 6.8753$ N/mm^2, $\bar{s} = 0.042$ mm, $n = 2.444$ and $G_f = 1.575$ N/mm.

considered twice. In the present study, according to BEM, concrete support is considered elastic. Hence, elastic compliance must be removed from Eq. (1). Initial (tangent) stiffness of interface law is given by:

$$K_0^{\mathrm{BS}} = \frac{\mathrm{d}\tau}{\mathrm{d}s}(s=0) = \frac{\bar{\tau}}{\bar{s}}\frac{n}{n-1}, \tag{2}$$

Hence, elastic stiffness of interface law for 2D BEM discretization can be obtained by subtracting elastic compliance of external concrete cover to the overall compliance defined in Eq. (2), i.e.:

$$\frac{1}{K_0^{\mathrm{BEM}}} = \frac{1}{K_0^{\mathrm{BS}}} - \frac{1}{K_{\mathrm{c}}} \tag{3}$$

where $K_{\mathrm{c}} = G_{\mathrm{c}}/h_{\mathrm{c}}$ is the stiffness of external concrete cover, with G_{c} being shear modulus and h_{c} thickness of concrete contributing to interface compliance. Cover thickness $h_{\mathrm{c}} = 25$–30 mm has been estimated in [68,56,39] by post-processing of experimental results.

Moreover, the value of fracture energy G_{f} of bond–slip law has been preserved, since that value is strictly related with the value of maximum transmissible force by an anchorage of infinite length [22]. Fracture energy of interface law (1) can be written as:

$$G_{\mathrm{f}} = \bar{\tau}\bar{s}\pi\left(\frac{1}{n-1}\right)^{\left(1-\frac{2}{n}\right)}\csc\left(\frac{2\pi}{n}\right). \tag{4}$$

Hence, for a given value of K_0^{BEM} (from Eq. (3)) and G_{f} (from experimental results), parameters $\bar{s}$ and n of interface law for 2D BEM discretization can be easily obtained from Eqs. (2) and (4). The corresponding interface law is reported in Fig. 1. In the same figure, a bilinear law is also depicted, which has been adopted in numerical examples for comparisons. It has been obtained by prescribing the same peak values $(\bar{\tau}, \bar{s})$ and fracture energy G_{f} of power fractional law adopted in the present study.

2.4. Further considerations

As well known, debonding is not a pure mode II failure mode, due to the presence of ''peeling stresses'', i.e. traction stresses normal to the interface. Hence, peak shear stress $\bar{\tau}$ can be smaller than maximum shear stress in pure mode II condition. Some rules have been proposed to define the peak shear stress in FRP–concrete connections, usually based on Mohr–Coulomb criterion [11], but they have not been at present experimentally validated. Difficulties are due to the fact that peeling stresses exhibit a very sharp gradient along the reinforcement and vanish few millimetres far from the end of anchorage. Hence, due to heterogeneity of concrete, failure criteria based on local stresses may be not appropriate. Pan and Leung [47] conducted a series of experimental tests under shear/peeling condition. They proposed a non-linear interface model where shear behavior depends on maximum peeling stress of the interface, while peeling behavior is assumed independent of shear stresses. Very often, due to the lack of experimental studies, shear and opening law are considered independent (see for instance [45,66]). A fully coupled model for joints between cementitious materials based on plastic-damage theory can be found in [34], even if the model has not been tested for joints under combined shear and tension.

Nevertheless, if the interface law is calibrated from experimental data, reduction of peak shear stress due to peeling stresses is already included in a simplified form. Of course, this interface law is valid when the anchorage is subjected to prevailingly mode II condition. Therefore, in the present analysis, a linearly elastic law is adopted for normal stress-transverse displacement relation, $\sigma = k_{\mathrm{p}}w$, where the adhesive stiffness is $k_{\mathrm{p}} = E_{\mathrm{g}}/h_{\mathrm{g}}$, E_{g} and h_{g} being elastic modulus and thickness of the adhesive layer, respectively.

Finally, denoting with $\mathbf{p} \overset{\mathrm{def}}{=} \{\sigma, \tau\}$ the cohesive traction vector and with $\mathbf{w} \overset{\mathrm{def}}{=} \{w, s\}$ the interface relative displacement vector, interface constitutive equation can be written in incremental form as:

$$\dot{\mathbf{p}} = -\widehat{\mathcal{D}}_t(\mathbf{w})\dot{\mathbf{w}} \tag{5}$$

where $\widehat{\mathcal{D}}_t(\mathbf{w})$ is the tangent stiffness matrix of the cohesive law and overhead dot denotes derivative with respect to t.

3. Cohesive interface and BIEs incremental formulation

3.1. General statements

We consider two homogeneous isotropic elastic bodies occupying the domains Ω_1 and Ω_2 (see Fig. 2), representing the undistorted natural reference configuration of two solids, bounded by exterior Lipschitz boundaries Γ^1, Γ^2 with outward unit normal $\mathbf{n}^1$ and $\mathbf{n}^2$, respectively, and connected by a cohesive interface $\Gamma_c = \Gamma^1 \cap \Gamma^2$. Domain boundaries Γ^i, $i = 1, 2$, are divided into three parts corresponding to different boundary or interface conditions to be imposed: $\Gamma^i = \Gamma^i_D \cup \Gamma^i_N \cup \Gamma^i_c$, where Γ^i_c is the portion of cohesive interface Γ_c belonging to the boundary Γ^i, whereas Γ^i_N, Γ^i_D are boundary portions where Neumann and Dirichlet boundary conditions must be imposed, respectively, i.e., $\mathbf{p}_i = \boldsymbol{\sigma}(\mathbf{u}_i)\mathbf{n}^i \equiv \bar{\mathbf{p}}_i$, on Γ^i_N, (where $\boldsymbol{\sigma}$ is the Cauchy stress tensor), and $\mathbf{u}_i \equiv \bar{\mathbf{u}}_i$ on Γ^i_D. Basic hypothesis of small displacements and strains implies:

$$\mathbf{n}^1(\mathbf{x}) = -\mathbf{n}^2(\mathbf{x}) = \mathbf{n}_c(\mathbf{x}), \quad \mathbf{x} \in \Gamma_c; \tag{6}$$

and equilibrium condition reads:

$$\mathbf{p}_1(\mathbf{x}) = -\mathbf{p}_2(\mathbf{x}), \quad \mathbf{x} \in \Gamma_c. \tag{7}$$

Moreover, we consider here the following assumptions: interface Γ_c is the locus of possible displacement discontinuities $\mathbf{w}$, and equilibrium between tractions across the interface is satisfied. According to the definition (6) of normal $\mathbf{n}_c(\mathbf{x})$ along Γ_c, the relative opening displacement is defined:

$$\mathbf{w}(\mathbf{x}, t) = \mathbf{u}_1(\mathbf{x}_1(t)) - \mathbf{u}_2(\mathbf{x}_2(t)), \quad \mathbf{x}_i \in \Gamma^i_c; \quad \mathbf{w}(\mathbf{x}, 0) = \mathbf{0}. \tag{8}$$

From Eqs. (6) and (7) we define for all $\mathbf{x} \in \Gamma_c$: $\mathbf{p}_c(\mathbf{x}) = \mathbf{p}_1(\mathbf{x})$ where $\mathbf{p}_c(\mathbf{x})$ is the traction on the interface. As a further assumption in the problem formulation, cohesive tractions $\mathbf{p}_c$ and relative displacements $\mathbf{w}$ at point $\mathbf{x} \in \Gamma_c$ are related by a non-linear cohesive law $\mathbf{p}_c = \mathbf{p}_c(\mathbf{w}(\mathbf{x}, t))$. Moreover we suppose that quasi-static external tractions $\bar{\mathbf{p}}_i(\mathbf{x}, t) = \lambda_p(t)\tilde{\mathbf{p}}_i(\mathbf{x})$ imposed on Γ^i_N and displacements $\bar{\mathbf{u}}_i(\mathbf{x}, t) = \lambda_u(t)\tilde{\mathbf{u}}_i(\mathbf{x})$ assigned on Γ^i_D of each domain Ω_i, $i = 1, 2$, are both products of a function of $\mathbf{x}$ and a function of t, where the second one plays the role of a load multiplier.

3.2. Incremental boundary integral equations

We define, with reference to general functions ψ_i and ϕ_i, the standard boundary integral operators, at $\mathbf{x} \in \Gamma^i$, i.e. the single and double layer potential operators [67]:

$$(\mathcal{V}^i\psi_i)(\mathbf{x}) = \int_{\Gamma^i} U^i(\mathbf{x}, \mathbf{y})\psi_i(\mathbf{y})\mathrm{d}s_\mathbf{y}, \quad (\mathcal{K}^i\phi_i)(\mathbf{x}) = \int_{\Gamma^i} T_{i,\mathbf{y}}U^i(\mathbf{x}, \mathbf{y})\phi_i(\mathbf{y})\mathrm{d}s_\mathbf{y}, \tag{9}$$

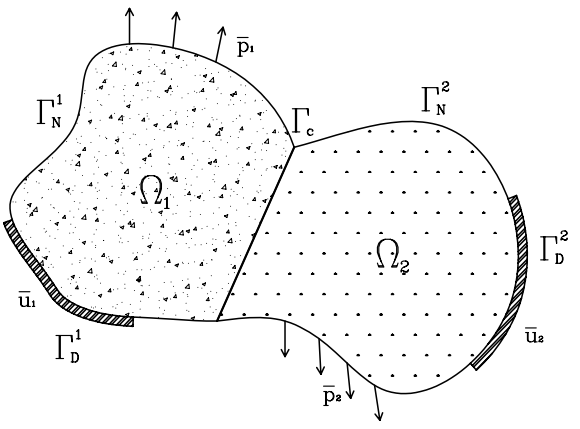

Fig. 2. Two domains connected by a cohesive interface Γ_c: the notation adopted.

the adjoint double layer potential and the hypersingular integral operator:

$$(\mathcal{K}'^i\psi_i)(\mathbf{x}) = \int_{\Gamma^i} T_{i,\mathbf{x}}U^i(\mathbf{x},\mathbf{y})\psi_i(\mathbf{y})\mathrm{d}s_\mathbf{y}, \quad (\mathcal{D}^i\phi_i)(\mathbf{x}) = T_{i,\mathbf{x}}\int_{\Gamma^i} T_{i,\mathbf{y}}U^i(\mathbf{x},\mathbf{y})\phi_i(\mathbf{y})\mathrm{d}s_\mathbf{y}. \tag{10}$$

Moreover, the operator $T_{i,\mathbf{y}}$ denotes the traction operator on Γ^i with differentiation with respect to $\mathbf{y}$, and $T_{i,\mathbf{y}}U^i(\mathbf{x},\mathbf{y})$ is the boundary stress tensor of the fundamental solution $U^i(\mathbf{x},\mathbf{y})$ of the linear elastic problem that we assume to exist for each subdomain Ω_i (see [48]). Operators $\mathcal{K}$ and $\mathcal{K}'$ are defined as Cauchy singular integrals and $\mathcal{D}$ is defined as a hypersingular finite part integral in the sense of Hadamard [59], i.e. the finite part of an asymptotic expansion. Finally, the operator $\mathcal{V}^i$ is weakly singular and the integral is defined in the classical Lebesgue sense.

The mapping properties of all local boundary integral operators defined above are well known (see [17]). Then, the incremental form of the standard boundary integral equation system related to the Dirichlet–Neumann problem on the ith domain, $i = 1, 2$, reads (see [54,25]):

$$\begin{aligned} &\mathcal{V}^i_{\mathrm{DD}}\dot{\mathbf{p}}_i - \mathcal{K}^i_{\mathrm{ND}}\dot{\mathbf{u}}_i + \mathcal{V}^i_{\mathrm{cD}}\dot{\mathbf{p}}_{i,c} - \mathcal{K}^i_{\mathrm{cD}}\dot{\mathbf{u}}_{i,\mathrm{c}} = \mathbf{f}^i_{\mathrm{D}} \quad \text{on } \Gamma^i_{\mathrm{D}},\\ &-\mathcal{K}'^i_{\mathrm{DN}}\dot{\mathbf{p}}_i + \mathcal{D}^i_{\mathrm{NN}}\dot{\mathbf{u}}_i - \mathcal{K}'^i_{\mathrm{cN}}\dot{\mathbf{p}}_{i,c} + \mathcal{D}^i_{\mathrm{cN}}\dot{\mathbf{u}}_{i,\mathrm{c}} = \mathbf{f}^i_{\mathrm{N}} \quad \text{on } \Gamma^i_{\mathrm{N}}, \end{aligned} \tag{11}$$

where

$$\mathbf{f}^i_{\mathrm{D}} = \left(\frac{1}{2}I + \mathcal{K}^i_{\mathrm{DD}}\right)\dot{\bar{\mathbf{u}}}_i - \mathcal{V}^i_{\mathrm{ND}}\dot{\bar{\mathbf{p}}}_i, \quad \mathbf{f}^i_{\mathrm{N}} = \left(-\frac{1}{2}I + \mathcal{K}'^i_{\mathrm{NN}}\right)\dot{\bar{\mathbf{p}}}_i - \mathcal{D}^i_{\mathrm{DN}}\dot{\bar{\mathbf{u}}}_i.$$

Subscripts ab (where a, $b = \mathrm{D}$, N, c denote the Dirichlet, Neumann and interface portion of the boundary) mean integration over Γ^i_a and evaluation over Γ^i_b. The displacement and traction BIEs (11), for the two faces of Γ_c are:

$$\begin{aligned} &\mathcal{V}^i_{\mathrm{Dc}}\dot{\mathbf{p}}_i - \mathcal{K}^i_{\mathrm{Nc}}\dot{\mathbf{u}}_i + \mathcal{V}^i_{\mathrm{cc}}\dot{\mathbf{p}}_{i,c} - \left(\tfrac{1}{2}I + \mathcal{K}^i_{\mathrm{cc}}\right)\dot{\mathbf{u}}_{i,\mathrm{c}} = \mathbf{f}^i_{\mathrm{Dc}} \qquad \text{on } \Gamma^i_{\mathrm{c}},\\ &-\mathcal{K}'^i_{\mathrm{Dc}}\dot{\mathbf{p}}_i + \mathcal{D}^i_{\mathrm{Nc}}\dot{\mathbf{u}}_i + \left(\tfrac{(-1)^{i-1}}{2}I - \mathcal{K}'^i_{\mathrm{cc}}\right)\dot{\mathbf{p}}_{i,c} + \mathcal{D}^i_{\mathrm{cc}}\dot{\mathbf{u}}_{i,\mathrm{c}} = \mathbf{f}^i_{\mathrm{Nc}} \quad \text{on } \Gamma^i_{\mathrm{c}}, \end{aligned} \tag{12}$$

where

$$\mathbf{f}^i_{\mathrm{Dc}} = -\mathcal{V}^i_{\mathrm{Nc}}\dot{\bar{\mathbf{p}}}_i + \mathcal{K}^i_{\mathrm{Dc}}\dot{\bar{\mathbf{u}}}_i, \quad \mathbf{f}^i_{\mathrm{Nc}} = \mathcal{K}'^i_{\mathrm{Nc}}\dot{\bar{\mathbf{p}}}_i - \mathcal{D}^i_{\mathrm{cc}}\dot{\bar{\mathbf{u}}}_i.$$

In Eq. (12), for $i = 2$, the normal at the field point has been chosen as inward. Now, let us define two new vector fields on the interface, the incremental mean displacement $\dot{\mathbf{v}}(\mathbf{x},t) = \frac{1}{2}[\dot{\mathbf{u}}_1(\mathbf{x}_1(t)) + \dot{\mathbf{u}}_2(\mathbf{x}_2(t))]$ and the incremental half opening displacement $\dot{\mathbf{z}}(\mathbf{x},t) = \frac{1}{2}[\dot{\mathbf{u}}_1(\mathbf{x}_1(t)) - \dot{\mathbf{u}}_2(\mathbf{x}_2(t))] = \frac{1}{2}\dot{\mathbf{w}}(\mathbf{x},t)$. The interface constitutive equation can be written in an incremental form making use of the tangent matrix of the cohesive law, denoted with $\widehat{\mathcal{D}}_t$, as (see Eq. (5)):

$$\dot{\mathbf{p}}_c(\mathbf{x},t) = 2\widehat{\mathcal{D}}_t(\mathbf{z}(\mathbf{x},t))\dot{\mathbf{z}}(\mathbf{x},t). \tag{13}$$

Finally, considering a suitable linear combination between Eqs. (11) and (12), the definition of vectors $\dot{\mathbf{v}}$, $\dot{\mathbf{z}}$ and Eq. (13), we obtain a system giving the incremental problem of two domains connected by a cohesive interface in the form (see [54]):

$$\mathbf{N}(\boldsymbol{\zeta}(t))\dot{\boldsymbol{\zeta}}(t) = \mathbf{F}(\boldsymbol{\zeta}(t),t) \tag{14}$$

where

$$\mathbf{N}(\boldsymbol{\zeta}(t)) = \begin{bmatrix} \mathcal{V}^1_{\mathrm{DD}} & -\mathcal{K}^1_{\mathrm{ND}} & 0 & 0 & -\mathcal{K}^1_{\mathrm{cD}} & \mathcal{C}^1_{\mathrm{cD}}[\boldsymbol{\zeta}(t)]\\ -\mathcal{K}'^1_{\mathrm{DN}} & \mathcal{D}^1_{\mathrm{NN}} & 0 & 0 & \mathcal{D}^1_{\mathrm{cN}} & \mathcal{C}^1_{\mathrm{cN}}[\boldsymbol{\zeta}(t)]\\ 0 & 0 & \mathcal{V}^2_{\mathrm{DD}} & -\mathcal{K}^2_{\mathrm{ND}} & -\mathcal{K}^2_{\mathrm{cN}} & \mathcal{C}^2_{\mathrm{cD}}[\boldsymbol{\zeta}(t)]\\ 0 & 0 & -\mathcal{K}'^2_{\mathrm{DN}} & \mathcal{D}^2_{\mathrm{NN}} & \mathcal{D}^2_{\mathrm{cN}} & \mathcal{C}^2_{\mathrm{cN}}[\boldsymbol{\zeta}(t)]\\ -\mathcal{K}'^1_{\mathrm{Dc}} & \mathcal{D}^1_{\mathrm{Nc}} & \mathcal{K}'^2_{\mathrm{Dc}} & -\mathcal{D}^2_{\mathrm{Nc}} & \mathcal{C}^{11}_{\mathrm{cc}} & \mathcal{C}^{12}_{\mathrm{cc}}[\boldsymbol{\zeta}(t)]\\ \mathcal{C}^1_{\mathrm{Dc}}[\boldsymbol{\zeta}(t)] & \mathcal{C}^1_{\mathrm{Nc}}[\boldsymbol{\zeta}(t)] & \mathcal{C}^2_{\mathrm{Dc}}[\boldsymbol{\zeta}(t)] & \mathcal{C}^2_{\mathrm{Nc}}[\boldsymbol{\zeta}(t)] & \mathcal{C}^{21}_{\mathrm{cc}}[\boldsymbol{\zeta}(t)] & \mathcal{C}^{22}_{\mathrm{cc}}[\boldsymbol{\zeta}(t)] \end{bmatrix}. \tag{15}$$

The components of unknown vector $\dot{\boldsymbol{\zeta}}(t) = [\dot{\mathbf{p}}_1\, \dot{\mathbf{u}}_1\, \dot{\mathbf{p}}_2\, \dot{\mathbf{u}}_2\, \dot{\mathbf{v}}\, \dot{\mathbf{z}}]^{\mathrm{T}}$ are tractions $\dot{\mathbf{p}}_i$ on Dirichlet boundaries Γ^i_{D}, displacements $\dot{\mathbf{u}}_i$ on Neumann boundaries Γ^i_{N}, mean displacement $\dot{\mathbf{v}}$ and relative half opening displacement $\dot{\mathbf{z}}$ on the cohesive interface Γ_{c} in their incremental form. Moreover:

$$\mathbf{f}(\boldsymbol{\zeta}(t), t) = \left[\mathbf{f}^1_{\mathrm{D}} \quad \mathbf{f}^1_{\mathrm{N}} \quad \mathbf{f}^2_{\mathrm{D}} \quad \mathbf{f}^2_{\mathrm{N}} \quad [\mathbf{f}^1_{\mathrm{Nc}} - \mathbf{f}^2_{\mathrm{Nc}}] \quad \left[\widehat{\mathcal{D}}^{\mathrm{T}}_t(\boldsymbol{\zeta}(t))(\mathbf{f}^1_{Dc} - \mathbf{f}^2_{\mathrm{Dc}}) + \mathbf{f}^1_{\mathrm{Nc}} + \mathbf{f}^2_{\mathrm{Dc}}\right]\right]^{\mathrm{T}}, \tag{16}$$

and terms $\mathcal{C}^i_{ab}$, $\mathcal{C}^{ij}_{ab}$ are combinations of integral operators previously defined and of cohesive tangent stiffness matrix $\widehat{\mathcal{D}}_t$:

$$\begin{aligned}
&\mathcal{C}^j_{\mathrm{cD}}[\boldsymbol{\zeta}(t)] = \mathcal{V}^j_{\mathrm{cD}}\widehat{\mathcal{D}}_t(\boldsymbol{\zeta}(t)) - \mathcal{K}^j_{\mathrm{cD}}, \quad \mathcal{C}^j_{\mathrm{cN}}[\boldsymbol{\zeta}(t)] = -\mathcal{K}'^j_{\mathrm{cN}}\widehat{\mathcal{D}}_t(\boldsymbol{\zeta}(t)) - \mathcal{D}^j_{\mathrm{cN}}, \quad j = 1, 2;\\
&\mathcal{C}^{11}_{\mathrm{cc}} = \sum_{j=1}^{2}(-1)^{j-1}\mathcal{D}^j_{\mathrm{cc}}, \mathcal{C}^{12}_{\mathrm{cc}}[\boldsymbol{\zeta}(t)] = \sum_{j=1}^{2} -\mathcal{K}'^j_{\mathrm{cc}}\hat{\mathcal{D}}_t(\boldsymbol{\zeta}(t)) + (-1)^j\mathcal{D}^j_{\mathrm{cc}},\\
&\mathcal{C}^{22}_{\mathrm{cc}}[\boldsymbol{\zeta}(t)] = \sum_{j=1}^{2}\widehat{\mathcal{D}}^{\mathrm{T}}_t(\boldsymbol{\zeta}(t))\mathcal{V}^j_{\mathrm{cc}}\widehat{\mathcal{D}}_t(\boldsymbol{\zeta}(t)) + (-1)^j\widehat{\mathcal{D}}^{\mathrm{T}}_t(\boldsymbol{\zeta}(t))\mathcal{K}^j_{\mathrm{cc}}\\
&\qquad - (-1)^j\mathcal{K}'^j_{\mathrm{cc}}\hat{\mathcal{D}}_t(\boldsymbol{\zeta}(t)) + (-1)^{j-1}\mathcal{D}^j_{\mathrm{cc}} + \widehat{\mathcal{D}}_t(\boldsymbol{\zeta}(t)) - \widehat{\mathcal{D}}^{\mathrm{T}}_t(\boldsymbol{\zeta}(t)).
\end{aligned} \tag{17}$$

For a complete description of these blocks and further details, the reader is referred to [25]. The following result holds [54]: if the tangent matrix of the cohesive law $\widehat{\mathcal{D}}_t$ is symmetric, the integral operator $\mathbf{N}$ is symmetric with respect to the usual bilinear form:

$$(\mathbf{N}\dot{\boldsymbol{\zeta}}, \dot{\boldsymbol{\xi}})_{L^2(\Gamma)} = (\dot{\boldsymbol{\zeta}}, \mathbf{N}\dot{\boldsymbol{\xi}})_{L^2(\Gamma)}. \tag{18}$$

Problem (14), equipped with an initial condition for $t = 0$ for the unknown vector $\boldsymbol{\zeta}(t)$ (for instance $\boldsymbol{\zeta}(t) = \mathbf{0}$), admits a unique solution under the hypothesis of invertibility for the operator $\mathbf{N}$. This condition holds if the interface law is stable in a second order sense (i.e. $\widehat{\mathcal{D}}_t$ is not negative definite). In this case, a semi-discretization with respect to t can be performed with standard adaptive explicit one-step methods. Then, for discretization in space, in order to apply the symmetric Galerkin boundary element method (see [10]), a family of finite-dimensional subspaces $S_{h,d}$ is defined on the boundary. Following well-known procedures, boundaries Γ^1, Γ^2 and interface Γ_{c} are discretized into boundary elements. On each boundary element, tractions, displacements on Γ^1, Γ^2, as well as mean displacement $\mathbf{v}$ and displacement discontinuity $\mathbf{z}$ over the interface Γ_{c} are interpolated from nodal values using polynomial shape functions. In the present problem, the space of piecewise polynomials $S_{h,d}$ is used as approximating subspaces for the approximation of $\mathbf{u}_i$ on Γ^i_{N}, $\mathbf{p}_i$ on Γ^i_{D} and $\mathbf{v}$, $\mathbf{z}$ on Γ_{c}.

3.3. Solution by arc length technique

Consider the non-linear incremental problem defined in Eq. (14), where the response is obtained for $\mathbf{p}$ varying from a null initial value and evolving quasi statically in time by means of a load factor $\lambda(t)$ in the form $\bar{\mathbf{p}}_i(\mathbf{x}, t) = \lambda(t)\tilde{\mathbf{p}}_i(\mathbf{x})$.

In the spirit of arc length method [51], an additional equation relating $\dot{\boldsymbol{\zeta}}(t)$ to the infinitesimal increment of the unknown load factor $\lambda(t)$ is introduced. Then, problem (14) is transformed as

$$\begin{cases}
\mathbf{N}(\boldsymbol{\zeta}(t))\dot{\boldsymbol{\zeta}}(t) = \dot{\lambda}(t)\mathbf{f}(\boldsymbol{\zeta}(t)) \quad t \in [0, t_{\mathrm{f}}]\\
\|\dot{\boldsymbol{\zeta}}(t)\|^2_2 + |\dot{\lambda}(t)|^2 = 1\\
\boldsymbol{\zeta}(0) = \boldsymbol{\zeta}_0, \quad \lambda(0) = \lambda_0.
\end{cases} \tag{19}$$

Note that the operator $\mathbf{N}(\boldsymbol{\zeta}(t))$ is invertible if and only if $\dot{\lambda}(t) \neq 0$. In this case, a unique solution can be found if the sign of $\dot{\lambda}(t)$ is specified. Under these hypothesis, problem (19) can be rewritten in the following normal form:

$$\begin{cases}
\dot{\mathbf{y}}(t) = \mathbf{F}(t, \mathbf{y}(t)), \quad t \in [0, \bar{t}[\\
\mathbf{y}(0) = \mathbf{y}_0
\end{cases} \tag{20}$$

where

$$\mathbf{y}(t) = \begin{bmatrix}\boldsymbol{\zeta}(t)\\ \lambda(t)\end{bmatrix}, \quad \mathbf{F}(t, \mathbf{y}(t)) = \mathrm{sgn}[\dot{\lambda}(t)][1 + \|\mathbf{b}(\boldsymbol{\zeta}(t))\|^2_2]^{-1/2}\begin{bmatrix}\mathbf{b}(\boldsymbol{\zeta}(t))\\ 1\end{bmatrix},$$

with $\mathbf{b}(\boldsymbol{\zeta}(t)) = \mathbf{N}^{-1}(\boldsymbol{\zeta}(t))\mathbf{f}(\boldsymbol{\zeta}(t))$. In Eq. (20), $\bar{t}$ represents the first value of t such that $\dot{\lambda}(\bar{t}) = 0$, corresponding to the attainment of the limit point (see numerical examples). Integration in time cannot continue because the operator $\mathbf{N}$ fails to be invertible.

In the discretization phase, the following constraint is introduced in order to determine the sign of $\dot{\lambda}(t)$:

$$\dot{\lambda}(t)\mu_1(t) > 0, \tag{21}$$

where $\mu_1(t)$ denotes the smallest eigenvalue of the discrete operator $\mathbf{N}_h(\boldsymbol{\zeta}_h(t))$ evaluated with reference to the approximated solution $\boldsymbol{\zeta}_h(t)$. If $\dot{\lambda}(t) = 0$ at the n-step, problem (19) becomes:

$$\begin{cases} \mathbf{N}(\boldsymbol{\zeta}(\bar{t}))\dot{\boldsymbol{\zeta}}(\bar{t}) = \mathbf{0} \\ \|\dot{\boldsymbol{\zeta}}(\bar{t})\|_2^2 = 1. \end{cases} \tag{22}$$

In this case, the eigenvector $\mathbf{q}$ of the matrix $\mathbf{N}_h(\boldsymbol{\zeta}_h(\bar{t}))$ related to the null eigenvalue must be determined and normalized with respect to Euclidean norm. Also in this case, the "orientation" of $\mathbf{q}$ is not determined; therefore, the constraint $\mathbf{q} \cdot [\boldsymbol{\zeta}_h(t_n) - \boldsymbol{\zeta}_h(t_{n-1})] > 0$ is introduced in order to get over the limit point and to obtain the solution at t_{n+1}:

$$\boldsymbol{\zeta}_h(t_{n+1}) = \boldsymbol{\zeta}_h(t_n) + (t_{n+1} - t_n)\mathbf{q}, \quad \lambda(t_{n+1}) = \lambda(t_{n-1}). \tag{23}$$

Note that for $t > \bar{t}$ the sign of $\mu_1(t)$ changes and therefore the sign of $\dot{\lambda}(t)$ changes too, denoting a softening branch on the equilibrium paths (see the following section).

Huge efforts have been made in the last two decades in order to improve computational efficiency of the constraint Eq. (19)b – see [28] for an exhaustive review. In the present paper, a local control function, analogous to that proposed in [38], is used. Accordingly, only the unknowns related to the non-linear behavior are used in the control equation. Differently from all previously cited papers, the present formulation is differential in time and the solution is reached by (explicit) time integration strategies. The reader is referred to [25] for additional details, exploiting features of boundary integral equations and arc-length technique.

4. Simulation of FRP–concrete debonding problems via BEM

The proposed BE model for cohesive interfaces has been used to simulate FRP–concrete debonding tests. Two different test setups are considered, depicted in Figs. 3 and 12. Mechanical and geometrical properties of specimens considered in numerical simulations are reported in Tables 1–3. For FRP–concrete interface, the non-linear law reported in Fig. 1 has been adopted.

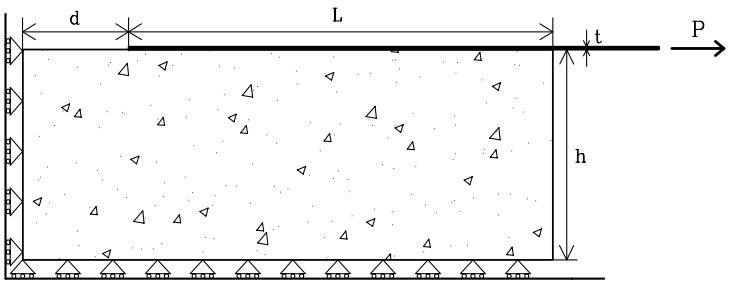

Fig. 3. Setup No. 1: Geometrical properties of specimens tested in [14].

Table 1
Setup no. 1: geometrical and mechanical properties of specimens tested in [14]

t (mm)	h (mm)	E_p (MPa)	E_c (MPa)	f_c (MPa)	b_p (mm)	b_c (mm)	d (mm)
1.016	152.4	108,380	33,640	36.4	25.4	152.4	50

Table 2
Setup no. 1: geometrical and mechanical properties of specimens considered in numerical simulations

t (mm)	h (mm)	E_p (MPa)	E_c (MPa)	f_c (MPa)	b_p (mm)	b_c (mm)	d (mm)
1.016	100	230,000	33,640	36.4	50	50	50

Table 3
Setup no. 2: geometrical and mechanical properties of specimens considered in numerical simulations

t (mm)	h (mm)	E_p (MPa)	E_c (MPa)	f_c (MPa)	b_p (mm)	b_c (mm)
1.016	150	230,000	33,640	36.4	50	50

4.1. Simulation of Setup No. 1 debonding test

Fig. 3 shows a typical configuration for pull–pull tests of FRP plates bonded to concrete. Left and bottom sides of the specimen are constrained in order to have no displacements in the direction normal to the surface and free displacements tangent to it. Two different numerical tests have been performed.

4.1.1. Comparison with experimental tests

Experimental tests reported in [14] have been simulated first. Geometrical and mechanical properties of the specimens are reported in Table 1. In these tests, FRP plate width (25.4 mm) was much smaller than concrete width. Nevertheless, in the simulations presented here, a plane stress problem has been considered. Boundary conditions are slightly different from those adopted in tests: an unconstrained front edge is adopted here. Since state of stress in concrete specimen is very small, the change of boundary conditions has no effects on results.

Comparison between experimental data and numerical results obtained through the present BE model are reported in Fig. 4a–d, for different bonding lengths. In each figure, strains in FRP plate along the bonding length are reported, for increasing values of applied force. The highest load corresponds to failure load obtained experimentally. For $L = 101.6$ mm bonding length debonding in numerical simulation occurred for a load smaller than in experiments; the corresponding strain profile is reported by dashed line. All figures show good agreement between numerical and experimental results both at low and high loading levels. Agreement at low loadings (the interface behavior being almost linear) means that initial interface stiffness is correctly defined. The agreement is very good also for high loadings, where plate debonding occurs: the change of curvature sign close to loaded plate end indicates that slip corresponding to maximum shear stress has been overcome and softening branch of interface law is involved.

Moreover, values of failure load as a function of bonding length are reported in Fig. 5. Experimental results are compared with numerical predictions obtained from the proposed BE solution and those given by a recently proposed 1D bond–slip model [56,22]. The two models give practically the same results, for both small and long bonding lengths. This circumstance confirms that the corresponding interface law for 2D domain discretization and bond–slip law proposed in [22] are actually equivalent. In the same figure, dashed line indicates failure loads obtained by adopting the bilinear interface law (also reported in Fig. 1) together with 2D BE method. It is clearly shown that failure loads using the bilinear law are significantly overestimated for small bonding lengths, even though the asymptotic values (for bonding length approaching infinity) are practically the same because the two different interface laws have the same value of fracture energy.

4.1.2. Other numerical tests

With reference to the same test setup and mechanical properties of specimens depicted in Fig. 3 and Table 2, plate width is 50 mm and different bond lengths have been considered ($L = 50$ mm, $L = 100$ mm and 200 mm). Load–displacement curves obtained from numerical simulations are reported in Fig. 6a–c, compared with results given by bond–slip 1D model [56,21]. Abscissa refers to relative axial displacement u between the initial and the final section of FRP plate (axial elongation of the plate).

It is worth noting that, for long bonding lengths (see Fig. 6c), snap-back branch occurs after the attainment of maximum load, due to elastic shortening of FRP plate when axial loading decreases during debonding. Of

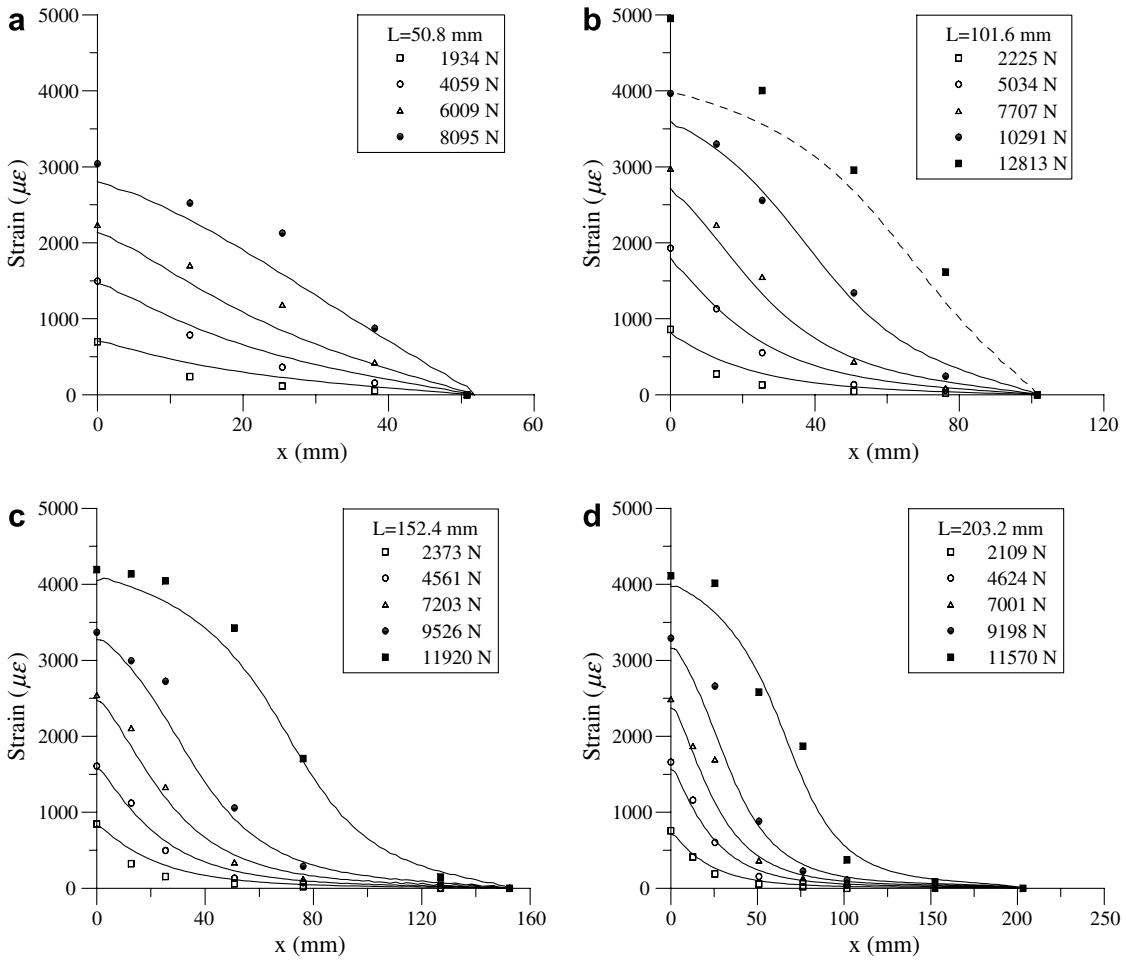

Fig. 4. Strains along FRP plates: experimental results from [14] and numerical simulations by BEM model: (a) $L = 50.8$ mm; (b) $L = 101.6$ mm; (c) $L = 152.4$ mm; (d) $L = 203.2$ mm.

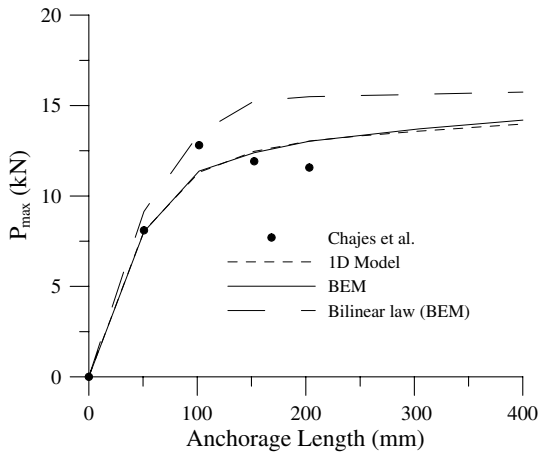

Fig. 5. Maximum transmissible force vs. bond length: experimental (from [14]) and numerical results by BEM model obtained with different interface laws and 1D bond–slip model ($b_p = 25.4$ mm).

course, this simulation cannot be performed with a standard force or displacement control procedure, and a more refined technique is required, such as the arc-length technique described in Section 3. Snap-back branch is not present in the case of shorter bonding lengths (see Figs. 6a and b).

For the 200 mm bonding length case, slip and shear stress profiles along the anchorage are reported in Figs. 7a and b. Curves refer to three different equilibrium points (A–C) indicated in Fig. 6c. Horizontal dashed line in Fig. 7a shows the slip value corresponding to peak shear stress of interface law reported in Fig. 1 ($\bar{s} = 0.0421$ mm). Hence, when slip is higher, softening branch in shear stress profile occurs (see Fig. 7b).

Furthermore, descending slip values that imply unloading behavior in the interface law may locally occur for the 200 mm bonding length case. However, this phenomenon involves only a limited portion of the interface (about 1/10 of the bonding length) and with very high slip values ($\geqslant 0.4$ mm), so giving negligible traction changes. For this reason, the adopted holonomic interface law may be considered to give sufficiently accurate results in the present case.

For the same case (200 mm bonding length), shear stresses in concrete specimen are reported in Figs. 8 and 9, for values of applied load equal to 40% and 100% of debonding load. Shear stress values in concrete have been evaluated by a post-processing procedure via the hypersingular Eq. (12), following [55]. Shear stresses along the interface between FRP plate and concrete are also depicted. These figures clearly show the growth of debonding along the interface between two materials. Shear stresses are always very high next to the interface and decrease rapidly through the concrete specimen depth. The singular points at the beginning and final sections of the anchorage, due to material discontinuity, are evident. Of course, stress distribution in the concrete specimen require the use of a 2D model and cannot be obtained from a single bond–slip 1D model. Moreover, the deformed specimen is schematically reported in Fig. 10.

Finally, for the 200 mm bonding length, load-plate elongation curves adopting, for the interface, the power fractional law reported in Eq. (1) and the bilinear law (see Fig. 1) are given in Fig. 11. The figure confirms that,

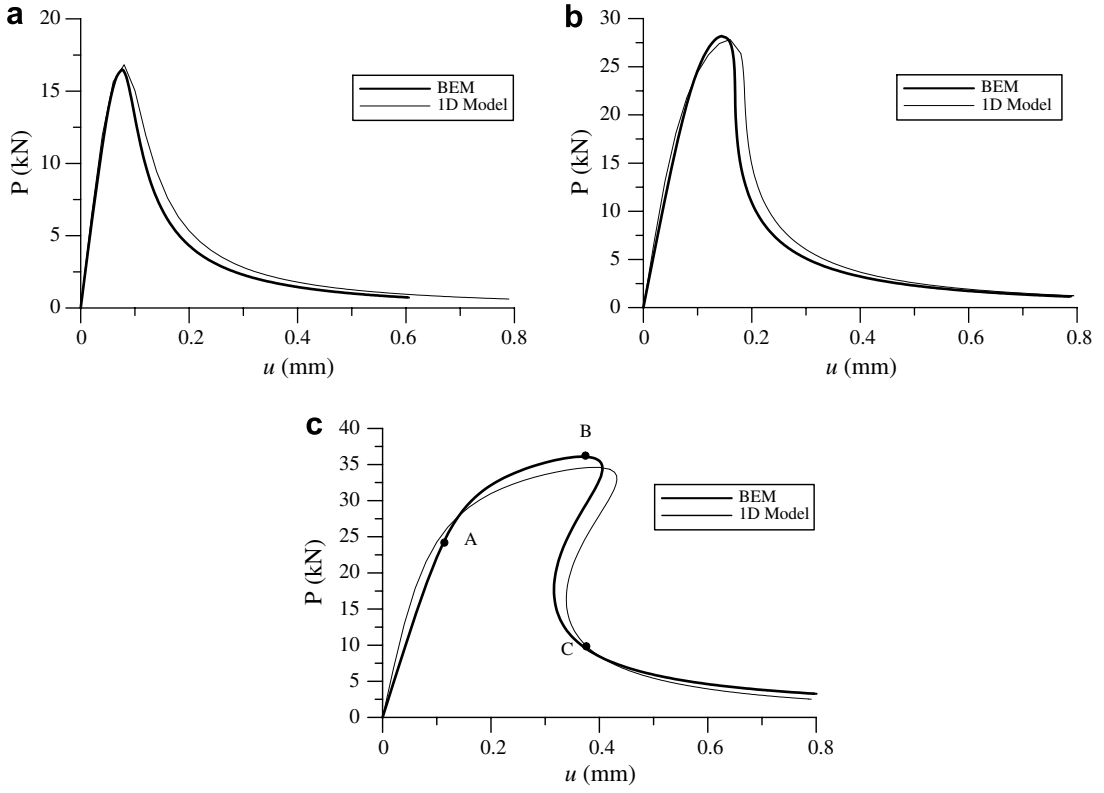

Fig. 6. Setup No. 1: Pull–pull delamination test: numerical simulations by BEM model and 1D bond–slip model. Axial load-elongation for: (a) $L = 50$ mm; (b) $L = 100$ mm; (c) $L = 200$ mm.

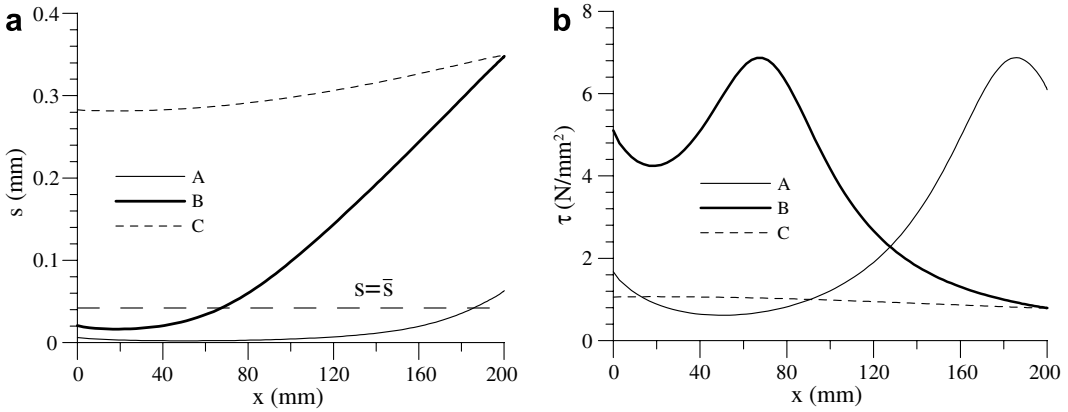

Fig. 7. Setup No. 1: (a) FRP–concrete slip s and (b) shear stress τ distributions along the interface.

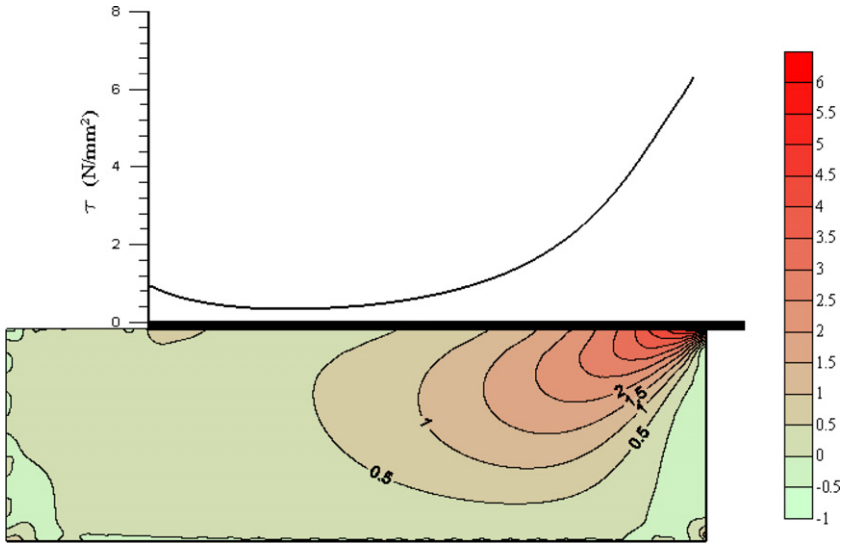

Fig. 8. Shear stress τ_{xy} for 40% of the maximum load level.

adopting the bilinear law, higher values of maximum load are predicted; moreover, snap-back branch is given by a (physically unrealistic) vertical straight line up to complete delamination.

4.2. Simulation of tests according to Setup No. 2

In No. 2 test setup, the specimen is symmetric and the load is applied at two external FRP plates (see Fig. 12). Moreover, both concrete and FRP plates are restrained at the left end section. This experimental setup has been proposed in [40] to obtain a stable delamination phenomenon. Bond length is $L = 600$ mm and other geometrical and mechanical properties are reported in Table 3.

The corresponding load-displacement curve is reported in Fig. 13. The figure clearly shows the transition between State 1 condition for low level loads (both stiffness contributions of concrete specimen and FRP plates are present) and State 2 condition after complete FRP debonding (FRP plates only contribute to specimen stiffness). Hence, in this case the post-delamination branch is stable and monotonically increasing. Figs. 14a and b show the profiles along the bonded length of FRP–concrete slip and shear stresses, with ref-

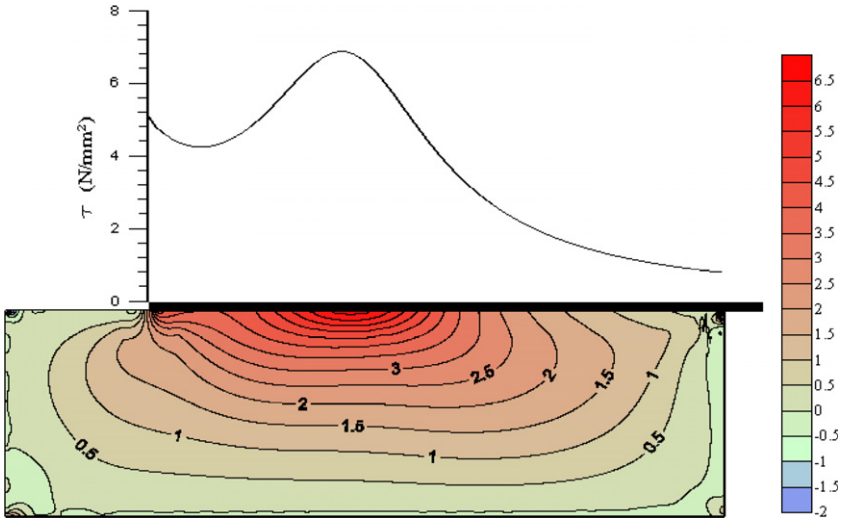

Fig. 9. Shear stress τ_{xy} for 100% of the maximum load level.

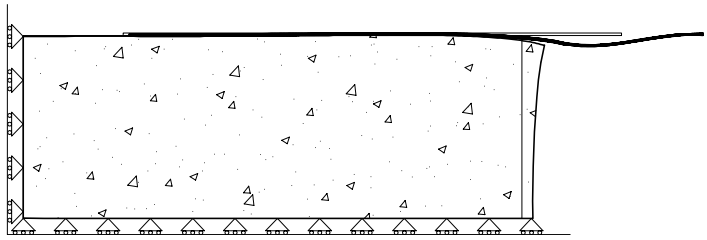

Fig. 10. Setup No. 1: deformed configuration.

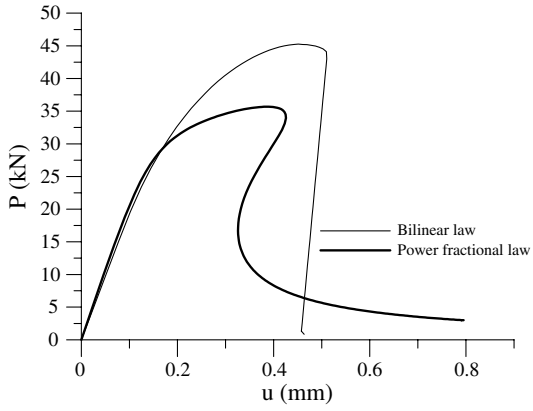

Fig. 11. Pull–pull FRP–concrete debonding test for $L = 200$ mm: solution obtained via BEM model with different interface laws ($b_p = 50$ mm).

erence to three different equilibrium points A–C indicated in Fig. 13. Point A indicates the beginning of delamination process, point C a condition where almost the whole plate is delaminated, and point B an intermediate condition. Fig. 14b clearly shows that, during delamination, the portion of plate contributing to the anchorage translates along the specimen from the (right) loaded end to the (left) restrained section.

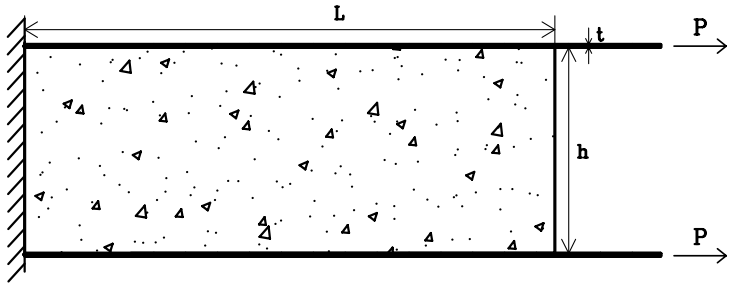

Fig. 12. Numerical simulation of FRP–concrete debonding test according to Setup No. 2.

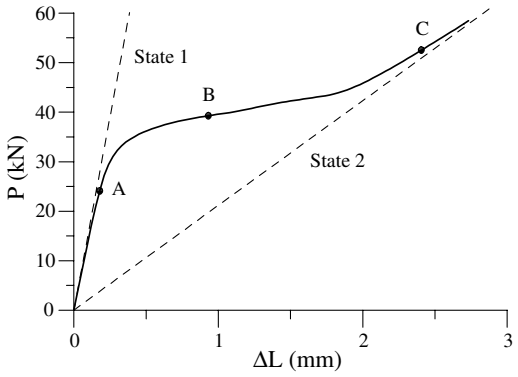

Fig. 13. Setup No. 2: Numerical simulation by BEM model. Load–displacement curve.

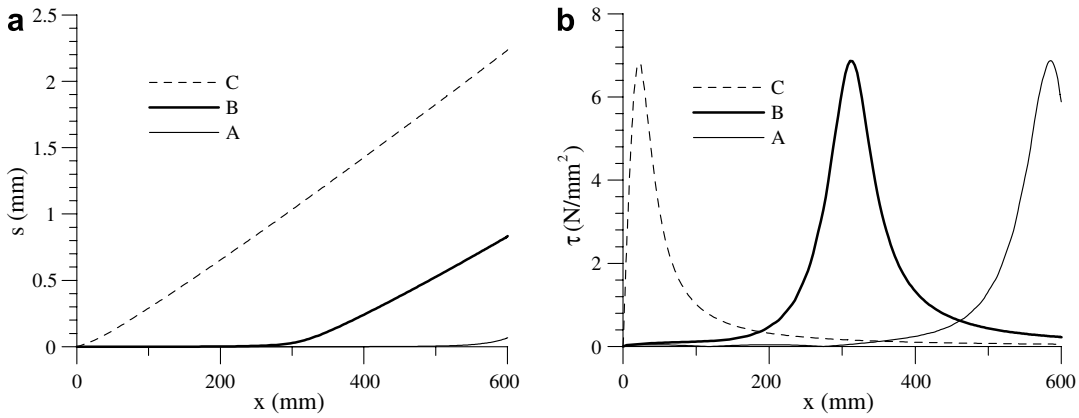

Fig. 14. Setup No. 2: (a) slip s and (b) shear stress τ distributions along the interface.

5. Conclusions

The problem of debonding of FRP plates externally bonded to concrete specimens is studied making use of boundary element method. In the proposed model, mode II cohesive crack model is adopted for the interface, whereas linear elasticity is used for the two materials outside the process zone (concrete and plate).

A non-linear constitutive FRP–concrete cohesive interface law suitable for 2D numerical simulations is used. The numerical model is based on symmetric Galerkin boundary element method, adopting the arc-length technique to follow the equilibrium path beyond its critical point, due to the softening behavior of the FRP–concrete interface law.

Some numerical simulations have been performed, concerning two different setups of delamination tests of FRP plates bonded on concrete substrate. Numerical results are found in good agreement with experimental results reported in the literature. Stress maps in concrete specimen are also obtained by post-processing results obtained via BEM over concrete specimen surface, showing the growth of debonding along the interface up to complete failure. The snap-back equilibrium branch outlined from numerical simulations confirms the very brittle failure mechanism associated with FRP debonding.

Acknowledgements

Financial supports of (Italian) C.N.R. (PAAS Grant 2001) and Department of Civil Protection (Reluis 2005-2008 Grant – Task 8: *Innovative materials for vulnerability mitigation of existing structures*) are gratefully acknowledged.

References

[1] Aimi A, Diligenti M, Freddi F. Numerical aspects in the SGBEM solution of softening cohesive interface problems. J Comput Appl Math; in press, doi:10.1016/j.cam.2006.10.053.
[2] Alfano G, Crisfield MA. Finite element interface models for the delamination analysis of laminated composites: mechanical and computational issues. Int J Numer Methods Engng 2001;50:1701–36.
[3] Aliabadi MH, Saleh AL. Fracture mechanics analysis of cracking in plain and reinforced concrete using the boundary element method. Engng Frac Mech 2002;69(2):267–80.
[4] Allix O, Corigliano A. Geometrical and interfacial non-linearities in the analysis of delamination in composites. Int J Solids Struct 1999;36:2189–216.
[5] Arrea M, Ingraffea AR. Mixed-mode crack propagation in mortar and concrete. Structural Engineering Report, No. 81-13; 1982.
[6] Barenblatt GI. The formulation of equilibrium cracks during brittle fracture, general ideas and hypothesis, axially symmetric cracks. Prikl Mater Mech 1959;23:434–44.
[7] Barenblatt GI. The mathematical theory of equilibrium cracks in brittle fracture. Adv Appl Mech 1962;7:55–129.
[8] Bazant ZP, Pfeiffer PA. Shear fracture tests of concrete. Mater Struct 1986;19:111–21.
[9] Bazant ZP, Planas J. Fracture and size effect in concrete and other quasibrittle materials. New directions in Civil Engineering. Boca Raton, FL: CRC Press; 1998.
[10] Bonnet M, Maier G, Polizzotto C. Symmetric Galerkin boundary element method. Appl Mech Rev 1998;51:669–704.
[11] Brosen K, Van Gemert D. Plate and shear design for external CFRP laminates. In: FRAMCOS-3 conference proceedings; 1998. p. 1793–804.
[12] Buyukozturk O, Hearing B. Crack propagation in concrete composites influenced by interface fracture parameters. Int J Solids Struct 1998;35(31–32):4055–66.
[13] Camacho GT, Ortiz M. Computational modelling of impact damage in brittle materials. Int J Solids Struct 1996;33:2899–938.
[14] Chajes MJ, Finch Wj, Januska TF, Thomson TA. Bond and force transfer of composite material plates bonded to concrete. ACI Struct J 1996;93:208–17.
[15] Chen T, Wang B, Cen Z, Wu Z. A symmetric Galerkin multi-zone boundary element method for cohesive crack growth. Engng Fract Mech 1999;63(5):591–609.
[16] Coronado CA, Lopez MM. Modeling of FRP–concrete bond using nonlinear damage mechanics. In: FRPRCS-7 conference proceedings; 2005.
[17] Costabel M. Boundary integral operators on Lipschitz domains: elementary results. SIAM J Math Anal 1988;19(3):613–26.
[18] De Borst R, Remmers JJC. Computational modelling of delamination. Compos Sci Technol 2006;66(6):713–22.
[19] Dugdale DS. Yielding of steel sheets containing slits. J Mech Phys Solids 1960;8:100–8.
[20] Erdogan F, Sih GC. On the crack extension in plates under plane loading transverse shear. J Basic Engng 1963;85:519–27.
[21] Ferracuti B, Savoia M, Mazzotti C. A numerical model for FRP–concrete delamination. Compos Part B: Eng 2006;37(4–5):356–64.
[22] Ferracuti B, Savoia M, Mazzotti C. Interface law for FRP–concrete delamination. Compos Struct 2007;80(7):523–31.
[23] Ferretti D, Savoia M. Serviceability behavior of R/C tensile members strengthened by FRP plates. Studies and researches; 2000. p. 95–124.
[24] Ferretti D, Savoia M. Cracking evolution in R/C tensile members strengthened by FRP plates. Engng Fract Mech 2003;70: 1069–83.
[25] Freddi F. Cohesive interface analysis via boundary integral equations. PhD thesis, University of Bologna, Italy. http://www.distart.ing.unibo.it/www2/studenti/post-laurea/dottorato/mds/index.php; 2004.
[26] Freddi F, Frémond M. Damage in domains and interfaces: a coupled predictive theory. J Mech Mater Struct 2006;1(7):1205–33.
[27] Freddi F, Royer-Carfagni G. Symmetric Galerkin BEM for bodies with unconstrained contours. Comput Methods Appl Mech Engng 2006;195(9–12):961–81.
[28] Geers MGD. Enhanced solution control for physically and geometrically non-linear problems. Part 1: the subplane control approach. Int J Numer Methods Engng 1999;46:177–204.

[29] Hellen TK. On the method of the virtual crack extension. Int J Numer Methods Engng 1975;9:187–207.
[30] Hillerborg A, Modeer M, Petersson PE. Analysis of crack formation and crack growth in concrete by means of fracture mechanics and finite elements. Cement Concr Res 1976;6:773–82.
[31] Hong KH, Chen JT. Derivations of integral equations of elasticity. ASCE J Engng Mech 1988;114:1028–44.
[32] Irwin GR. Analysis of stresses and strains near the end of a crack transversing a plate. ASME J Appl Mech 1957;24:361–6.
[33] Jansze W. Strengthening of reinforced concrete members in bending by externally bonded steel plates. PhD thesis, TU Delft, Delft; 1997.
[34] Jefferson AD. Plastic-damage model for interfaces in cementitious materials. ASCE J. Engng Mech 1998;124(7):775–82.
[35] Lu XZ, Teng JG, Ye LP, Jiang JJ. Bond-slip models for FRP sheet/plates bonded to concrete. Engng Struct 2005;27:920–37.
[36] Lu XZ, Ye LP, Teng JG, Jiang JJ. Meso-scale finite element model for FRP sheets/plates bonded to concrete. Engng Struct 2005;27:564–75.
[37] Malek AM, Saadatmanesh H, Ehsani MR. Prediction of failure load of R/C beams strengthened with FRP plate due to stress concentration at the plate end. ACI Struct. J 1998;95:142–52.
[38] May IM, Duan Y. A local arc-length procedure for strain softening. Comput Struct 1997;64:297–303.
[39] Mazzotti C, Ferracuti B, Savoia M. An experimental study on FRP–concrete delamination. In: FRAMCOS-5 conference proceedings, vol. 2; 2004. p. 795–802.
[40] Mazzotti C, Savoia M, Ferracuti B. A new set-up for FRP–concrete stable delamination test. In: FRPRCS-7 conference proceedings; 2005.
[41] McLean W. Strongly elliptic systems and boundary integral equations. New York: Cambridge University Press; 2000.
[42] Monti G, Renzelli M, P. FRP adhesion to uncracked and cracked concrete zones. In: Tan, K., editor, FRPRCS-6 conference proceedings, Singapore; 2003. p. 183–92.
[43] Neto P, Alfaiate J, Almeida JR, Pires EB. The influence of mode II fracture on concrete strengthened with CFRP. Comput Struct 2004;82(17–19):1495–502.
[44] Neves IB, Chabut M, Perruchot C, Chehimi MM, Benzarti K. Interfacial interactions of structural adhesive components with cement pastes: Studies by inverse gas chromatography (IGC). Appl Surf Sci 2004;238(1–4):523–9.
[45] Niu H, Karbhari V, Wu Z. Diagonal macro-crack induced debonding mechanisms in FRP rehabilitated concrete. Compos Part B: Eng 2006;37(7–8):627–41.
[46] Ortiz M, Pandolfi A. Finite deformation irreversible cohesive elements for three dimensional crack propagation analysis. Int J Numer Methods Engng 2000;47:675–8.
[47] Pan J, Leung CKY. Debonding along FRP–concrete interface under conbined pulling/peeling effects. Engng Fract Mech 2007;74:132–50.
[48] Pomp A. The Boundary-Domain integral method for elliptic systems. With an application to shells. Lecture Notes in Mathematics. Berlin: Springer-Verlag; 1998.
[49] Rabinovitch O. Fracture-mechanics failure criteria for RC beams strengthened with FRP strips – a simplified approach. Compos Struct 2004;64(3–4):479–92.
[50] Rice JR. A path independent integral and the approximate analysis of strain concentration by notches and cracks. ASME J Appl Mech 1957;24:361–6.
[51] Riks E. An incremental approach to the solution of snapping and buckling problems. Int J Solids Struct 1979;15:529–51.
[52] Roberts TM and Haji-Kazemi H. Theoretical study of the behavior of reinforced concrete beams strengthened by externally bonded steel plates. In: Proceedings of the Institution of Civil Engineers, vol. 2, London, UK; 1989. p. 39–55.
[53] Rybicki EF, Kanninen MF. A finite element calculation of stress intensity factors by a modified crack closure integral. Engng Frac Mech 1977;9:931–8.
[54] Salvadori A. A symmetric boundary integral formulation for cohesive interface problems. Comput Mech 2003;32(4–6):381–91.
[55] Salvadori A, Freddi F. Cohesive interfaces stress analysis via boundary integral equations. In: IABEM conference proceedings, UT Austin, TX, USA; 2002.
[56] Savoia M, Ferracuti B, Mazzotti C. Delamination of FRP plate/sheets used for strengthening of r/c elements. In: De Borst R, editor, Second international conference on Structural Engineering and Construction (ISEC-02),Rome, IT; 2003. p. 1375–81.
[57] Savoia M, Ferracuti B, Mazzotti C. Non linear bond–slip law for FRP–concrete delamination. In: Tan, K., editor, FRPRCS-6 conference proceedings, Singapore, 2003, p. 1–10.
[58] Savoia M, Mazzotti C, Ferracuti B. Mode II fracture energy and interface law for FRP concrete bonding with different concrete surface preparations. In FRAMCOS-6 conference proceedings, Catania, IT; 2007.
[59] Schwab C, Wendland W. Kernel properties and representations of boundary integral operators. Numer Math 1992;156:187–218.
[60] Smith JG, Teng J. Interfacial stresses in plated beams. Engng Struct 2001;23:857–71.
[61] Taljsten B. Strengthening of concrete prisms using the plate bonding technique. Int J Fract 1996;43:1–18.
[62] Teng JG, Chen JF, Smith ST, Lam L. FRP strengthened RC structures. UK: John Wiley and Sons; 2002.
[63] Teng JG, Yuan H, Chen JF. FRP-to-concrete interfaces between two adjacent cracks: Theoretical model for debonding failure. Int J Solids Struct 2006;43(18–19):5750–78.
[64] Toutanji H, Ortiz G. The effect of surface preparation on the bond interface between FRP sheets and concrete members. Compos Struct 2001;53:457–62.
[65] Volkersen O. Die nietkraftverteilung in zugbeanspruchenden nietverbindungen mit konstanten laschen-querschnitten. Luftfahrtforschung 1938;15:41–7.

[66] Wang J. Cohesive zone model of FRP–concrete interface debonding under mixed-mode loading. Int J Solids Struct; in press, doi:10.1016/j.ijsolstr.2007.02.042.
[67] Wendland WL. Variational methods for BEM. In: Morino L, Piva R, editors. Boundary integral methods (theory and applications). Springer-Verlag; 1990.
[68] Wu Z, Yuan H, Niu H. Stress transfer and fracture propagation in different kinds of adhesive joints. ASCE J Engng Mech 2002;128:562–73.
[69] Yang J, Ye J. Interfacial stresses in plated beams with cracks. Compos Struct 2002;57(1):125–34.
[70] Yuan H, Teng JG, Seracino R, Wu ZS, Yao J. Full-range behavior of FRP-to-concrete bonded joints. Engng Struct 2004;26:553–65.
[71] Zou Z, Reid SR, Li S. A continuum damage model for delamination in laminated composites. J Mech Phys Solids 2003;51:333–56.
[72] Zou Z, Reid SR, Soden PD, Li S. Mode separation of energy release rate for delamination in composite laminates using sublaminates. Int J Solids Struct 2001;38:2597–613.